Research Square

Preprints are preliminary reports that have not undergone peer review.
They should not be considered conclusive, used to inform clinical practice,
or referenced by the media as validated information.

Definable Two-Dimensional Mesoporous Polydopamine-Graphene Heterostructure as Multi-Functional Ion Redistributor for Ultrastable Sodium Metal Anodes

Jieqiong Qin
Dalian Institute of Chemical Physics
Haodong Shi
Dalian Institute of Chemical Physics
Kai Huang
Dalian Institute of Chemical Physics
Pengfei Lu
Dalian Institute of Chemical Physics
Pengchao Wen
Dalian Institute of Chemical Physics
Feifei Xing
Dalian Institute of Chemical Physics
Bing Yang
Dalian Institute of Chemical Physics https://orcid.org/0000-0003-3515-0642
Mao Ye
Dalian Institute of Chemical Physics https://orcid.org/0000-0002-7078-2402
Yan Yu
University of Science & Technology of China
Zhong-Shuai Wu (wuzs@dicp.ac.cn)
Dalian Institute of Chemical Physics https://orcid.org/0000-0003-1851-4803

Article

Keywords: two-dimensional (2D) mesoporous polydopamine-graphene (mPG) heterostructures, multi-functional ion redistributors, ultrastable sodium metal anodes

Posted Date: October 6th, 2020

DOI: https://doi.org/10.21203/rs.3.rs-74650/v1

License: This work is licensed under a Creative Commons Attribution 4.0 International License.
Read Full License

Version of Record: A version of this preprint was published at Nature Communications on October 1st, 2021. See the published version at https://doi.org/10.1038/s41467-021-26032-1.

Abstract

Sodium metal batteries are widely acknowledged as one of the most promising low-cost high-energy-density batteries, but limited by uncontrollable dendritic growth and short cyclability. Herein, two-dimensional (2D) mesoporous polydopamine-graphene (mPG) heterostructures with definable pore size and sheet thickness are demonstrated as multi-functional ion redistributors to realize ultrastable, dendrite-free Na metal anodes. Benefitting from abundant sodiophilic groups (-OH, C=O and -NH-), 2D nanoporous graphene, and ordered mesoporous ion channels in mPG, the Na metal anodes show high Coulombic efficiency of >99.5%, outstanding cyclability of ~2000 h, and unprecedented rate performance of 25 mA cm^{-2} with 25 mAh cm^{-2}, outperforming all the reported Na anodes stabilized by diversified strategies. What's more, the mPG based Na/$Na_3V_2(PO_4)_3$ full batteries deliver exceptionally enhanced cyclability (90% retention rate after 500 cycles) and rate capacity (75 mAh g^{-1} at 30 C), demonstrative of impressive potential of well-designed 2D mesoporous polymers for precisely regulating Na deposition.

Introduction

The rapid growth of portable electronics, electric vehicle, autonomous aircraft and smart grid has intensively stimulated the urgent requirements for low-cost, high-energy-density batteries[1–4]. Due to high theoretical capacity (1166 mAh g^{-1}), low redox potential (-2.714 V *vs*. standard hydrogen electrode), natural abundance and low price, metal sodium (Na) has been regarded as a highly competitive anode for next-generation rechargeable battery[5–9]. Unfortunately, its high reactive activity, large volume change, unstable solid electrolyte interface (SEI) and uncontrollable dendritic growth bring about low Coulombic efficiency, limited cyclability, and even safety risk for high-energy-density Na metal batteries, such as Na-S[10] and Na-O_2 batteries[11], substantially inhibiting their actual applications[5, 12–15]. To overcome the issues, various strategies, including tailoring electrolyte formulation (*e.g.*, highly concentrated electrolyte, fluoroethylene carbonate additive)[16, 17], using solid-state electrolytes (gel polymer with boron nitride, $Na_3Zr_2Si_2PO_{12}$)[18, 19], creating artificial SEI (*e.g.*, Al_2O_3, sodium benzenedithiolate, graphene)[20–22], and designing nanostructured Na anodes (*e.g.*, Na@O-functionalized carbon nanotube networks, Na@porous Al, Na@carbonized wood)[14, 23, 24], have been developed to suppress the growth of Na dendrites and realize stable and safe Na metal anodes. Nevertheless, these designs usually revealed single chemical or physical function for regulating Na dendrites, and faced high processing cost and limited scalability. Besides, constructing functional separators is considered as a more reliable and cost-effective way to realize uniform Na deposition from chemical molecule and physical structure levels[25–27].

From the viewpoint of molecular level, polymer brushes with abundant polar functional groups (*e.g.*, C = O, -OH, -COOH and N-H) can enhance the electrolyte wettability, provide robust SEI interface, and thus easily homogenize the alkali-metal ion distribution and nucleation[21, 28–32]. In particular, two-dimensional (2D) graphene-like polymer materials (*e.g.*, poly(N-isopropylacrylamide), polyacrylamide grafted graphene oxide (GO) and polypyrrole-GO heterostructure) with sheet-like structure, high specific surface area (SSA), abundant surface chemistry and outstanding mechanical flexibility, show tremendous advantage to

regulate alkali-metal deposition and physically restrain dendrite puncture[22, 28, 29, 33]. From the perspective of structure design, 2D defective GO and ordered mesoporous structure can serve as nanoporous buffer and ion channels to homogenize alkali-metal ions distribution and deposition[33]. Therefore, the reasonable construction of definable 2D mesoporous functional polymer heterostructure for realizing ultrastable, dendrite-free Na metal anodes from chemical molecule and physical structure levels is highly competitive yet remains elusive.

Herein, 2D mesoporous polydopamine-graphene (mPG) heterostructures with definable pore diameter and sheet thickness have been developed for ultrastable, high-capacity Na metal anodes. Using free-standing 2D substrate of graphene and variable mesoporous template of SiO_2 nanospheres, 2D sandwich-like mPG heterostructures with adjustable pore sizes (7, 12, 22 nm), tailored sheet thickness (14, 20, 28 nm), and high SSA (144, 157, 114 $m^2 g^{-1}$) are successfully synthesized *via* 2D GO based hard-template strategy. Owing to sodiophilic polydopamine surface, defective graphene layer, uniform mesoporous structure and high SSA, 2D mPG heterostructures can serve as multi-functional ion redistributors to endow Na metal anodes with superior Coulombic efficiency (> 99.5%), cycling stability (~ 2000 h at 1 mA cm^{-2} with 1 mAh cm^{-2}) and unprecedented rate performance (25 mA cm^{-2} with 25 mAh cm^{-2}). As a consequence, the mPG based Na/$Na_3V_2(PO_4)_3$ (NVP) full batteries demonstrate remarkably stable cyclability with 90% capacity retention rate over 500 cycles and outstanding rate capability showing a capacity of 75 mAh g^{-1} at 30 C (1 C = 117.6 mA g^{-1}).

Results

Fabrication and characterization of 2D mPG heterostructures. The synthesis process of 2D mPG heterostructures is schematically shown in Fig. 1a. First, the GO nanosheets modified by polydiallyldimethylammonium chloride are employed as 2D free-standing substrates. Then, monodispersed SiO_2 nanospheres with negative charge serve as mesoporous templates to orderly assemble on the surface of GO substrates through electrostatic adsorption. Afterwards, homogeneous polydopamine (Supplementary Scheme 1) layer is patterned on the surface of as-prepared SiO_2-GO nanosheets to form SiO_2-PGO nanosheets. Finally, 2D mPG heterostructures with defined mesopore size and sheet thickness are generated after hydrothermal treatment (defined as SiO_2-PG) and SiO_2 etching. It is worth noting that this template strategy can efficiently realize the strong coupling of sodiophilic polydopamine, defective graphene (Supplementary Fig. 1) and adjustable mesopores, which is highly conducive to construct multi-functional ion redistributors for dendrite-free Na metal anodes (Fig. 1b), as discussed below.

The microstructure and chemical composition of 2D mPG heterostructures are presented in Fig. 2. Taking mPG with 12 nm mesopores (mPG-12) nanosheets as example, scanning electron microscopy (SEM) image displays flat and uniform 2D morphology with lateral size ranging from 0.5 to 3 μm (Fig. 2a). Transmission electron microscopy (TEM) and high-resolution TEM (HRTEM) images clearly indicate homogeneous 2D mesoporous structure of mPG-12 nanosheets with uniformly ordered mesopores of ~

12 nm (Fig. 2b and 2c). Atomic force microscopy (AFM) image reveals 2D flat structure with a uniform thickness of ~ 20 nm (Fig. 2d). More importantly, the accurate patterning of mesoporous polydopamine on graphene surface with definable pore size and thickness can be precisely controlled, *e.g.*, by changing the size of SiO_2 template (Fig. 2e-h and Supplementary Fig. 2). Specially, mPG-7 nanosheets show uniform mesopores of ~ 7 nm and an average thickness of 14 nm, while mPG-22 nanosheets present ordered mesopores of ~ 22 nm and sheet thickness of ~ 28 nm. Meanwhile, non-mesoporous polydopamine-graphene (nPG) nanosheets are also synthesized (Supplementary Fig. 3) to highlight the importance of structure-directing SiO_2 templates. Moreover, N_2 adsorption and desorption isotherms of mPG-7, mPG-12, mPG-22, and nPG nanosheets represent type IV curves with H2-type hysteresis loop (Supplementary Fig. 4). Notably, mPG-12 nanosheets display larger SSA of 157 $m^2 g^{-1}$ than mPG-7 (144 $m^2 g^{-1}$), mPG-22 (114 $m^2 g^{-1}$) and nPG (54 $m^2 g^{-1}$) nanosheets (Supplementary Table 1). Further, the dominated mesopore sizes of 6.8 nm for mPG-7, 12.2 nm for mPG-12, and 18.6 nm for mPG-22 nanosheets are well validated by the pore size distribution (Fig. 2i), nearly consistent with TEM observation. Fourier transform infrared spectroscopy (FT-IR) spectrum of mPG-12 reveals the existence of double peaks at 2930 and 2863 cm^{-1} featuring the indole structure, the characteristic vibration peak at 1712 cm^{-1} assigning to quinone (C = O) groups, and two distinct peaks at 1572 and 1462 cm^{-1} attributing to C = C resonance vibration and N-H bending vibration (Supplementary Fig. 5), demonstrative of the hybridization of polydopamine and graphene in mPG-12[30, 34, 35]. Furthermore, X-ray photoelectron spectroscopy (XPS) of mPG-12 confirms three strong signals of C1s, N1s and O1s (Supplementary Fig. 6). The C1s spectrum is fitted by four characteristic peaks of 284.5 ± 0.1 eV for CH_x and sp^2-hybridized carbon, 285.7 ± 0.2 eV for C-O/C-N, 287.8 ± 0.2 eV for C = O, and 288.9 ± 0.2 eV for O-C = O (Fig. 2j)[34, 36, 37]. The O1s spectrum exhibits two peaks centered at 533.0 ± 0.2 eV for O-C and 531.3 ± 0.1 eV for O = C[34, 36, 37]. Moreover, the N1s spectrum reveals three peaks at 401.7 ± 0.1 for $-NH_2$, 400.0 ± 0.1 eV for -NH-, and 398.5 ± 0.1 eV for -N = functional groups, respectively[34, 36, 37]. It is evidenced that the mesoporous polydopamine layer is effectively grafted with graphene, and the abundant polar functional groups, *e.g.*, C = O, -OH and -NH-, are existed in 2D mPG heterostructure.

Calculation of sodiophilic nature and Na deposition behavior for mPG. To examine the effect of polar functional groups and 2D mesoporous structure on Na metal deposition, density functional theory (DFT) calculation and finite volume method (FVM) simulation were conducted. Figure 3a-c and Supplementary Fig. 7 display the binding energies and charge densities between Na atom and polydopmine, graphene, PP and Cu. It can be seen that the interaction between Na and Cu (-1.20 eV) or PP (-0.41 eV) is much weaker than that between Na and polydopmine, owing to abundant polar groups (C = O of -4.24 eV, -OH of -3.47 eV, -NH- of -3.37 eV). Thus, the sodiophilic nature of mPG coupled polydopmine and graphene with a high binding energy of -2.08 eV can serve as active site to realize more uniform ion transport and Na deposition. Furthermore, the effect of mesopore size of 2D mPG on Na ions distribution is investigated by FVM simulation. As shown in Fig. 3d and Supplementary Fig. 8, the migration of Na ions driven by electric field and diffusion flow through 20 layers of mPG nanosheets is taken into account for the simulation. With the shunting of 2D mesoporous structure in mPG, the distribution of Na ions becomes

increasingly uniform as ions migrate along the Y-axis, and achieves almost stability after four layers of mPG (Fig. 3e and Supplementary Fig. 9). The 2D mPG-7 reveals the lowest standard deviation whether with same amplitude and period or same fluctuation and period of Na ion distribution at the entrance, implying the smaller mesopores are more beneficial to the redistribution and uniformity of Na ions (Fig. 3f, g). However, electrochemical impedance spectroscopy (EIS) shows that mPG-12 possess lower charge transfer resistance (14.9 Ω) and higher Na ion diffusion coefficient (5.7×10^{-12} cm^2 s^{-1}), compared with mPG-7 (36.2 Ω and 2.7×10^{-13} cm^2 s^{-1}) and mPG-22 (32.9 Ω and 2.6×10^{-12} cm^2 s^{-1}), possibly because of larger SSA, appropriate meopore size and thickness for faster ion diffusion transport[38–40] (Supplementary Fig. 10). Taken the above into consideration, 2D mPG heterostructures (especially mPG-12) possess huge merits of serving as multi-functional redistributor to homogenize distribution of Na ions and prevent “tip effects” of Na deposition[33, 41].

Characterization and performance of mPG-12 redistributor for Na metal anode. Considering the unique advantages of 2D mPG heterostructures, we fabricated mPG-12 based PP (mPG-12@PP) hybrid separators for Na metal anodes and Na metal batteries. Compared with bare PP separator with plenty of large pores (~ 500 nm) and 25 μm thickness, mPG-12@PP separators exhibit uniform, layer-stacked film (only ~ 9 μm thickness) of 2D mPG-12 nanosheets on the surface of PP, while retain outstanding flexibility and well-defined pores (Fig. 4a-c and Supplementary Fig. 11, 12). Further, the contact angle of electrolyte on mPG-12@PP separator is ~ 8° (Fig. 4d), which is much lower than that on PP separator (31°), indicative of enhanced affinity of mPG-12@PP with electrolyte that is beneficial for Na ion diffusion[28, 42].

To highlight the importance of mesopores in mPG-12, nPG based PP (nPG@PP) separator was also assembled. The electrochemical performance of Na/Cu half cells with mPG-12@PP, nPG@PP and PP separators was first evaluated to illustrate Na deposition behavior. At a current density of 0.5 mA cm^{-2} with a cycling capacity of 0.5 mAh cm^{-2}, the Na/Cu cells with mPG-12@PP separator exhibit ultrastable plating/stripping process for 550 cycles (~ 1100 h) with a steady Coulombic efficiency of ~ 99.8%, which is better than that of nPG@PP (400 cycles with ~ 99.5% Coulombic efficiency) and PP separators (200 cycles with < 90.0% Coulombic efficiency) (Fig. 4e). It can be well explained by the enlarged plating-stripping curves (Fig. 4f), in which the Na/Cu cells with mPG-12@PP separator show the lowest nucleation overpotential of only 20 mV than those of Na/Cu cells with nPG@PP (60 mV) and PP (170 mV) separators. The reduced nucleation overpotential verifies the low interface resistance and enhanced Na ion transport kinetics through mPG-12@PP separator. Even at higher current density and areal capacity (4.0 mA cm^{-2} and 4.0 mAh cm^{-2}; 8.0 mA cm^{-2} and 8.0 mAh cm^{-2}), the Coulombic efficiency and cycling performance of Na/Cu cells with mPG-12@PP separator (~ 99.9% for 450 cycles; ~99.7% for 350 cycles) still outperform PP separator (~ 78.5% for 90 cycles; ~51.7% for 50 cycles), further demonstrating the superiority of mPG-12@PP separator for protecting Na metal anodes (Fig. 4g and Supplementary Fig. 13). To visually understand the impact of mPG-12@PP separator on Na plating/stripping process, the morphologies of Na metal anodes were traced by SEM (Supplementary Fig. 14). For the cell with bare PP separator, the anode exhibits obvious Na dendrites with loosely moss-

like structure at a Na loading of 1.0 mAh cm^{-2}. In a sharp contrast, mPG-12@PP separator endows Na metal anode with a rather uniform and smooth surface without obvious dendrites, and this morphology becomes denser upon an increased Na loading of 2.0 mAh cm^{-2}. The distinctive morphological transition of Na metal anodes with different separators demonstrates the key role of mPG-12 on efficient regulation of the Na ions distribution and Na deposition.

Furthermore, symmetric Na/Na cells were fabricated to assess the voltage hysteresis and cycling stability. Figure 4h exhibits the voltage-time curves of Na/Na cells with mPG-12@PP, nPG@PP and bare PP separators at 1 mA cm^{-2}, 1 mAh cm^{-2}. Notably, the cells with mPG-12@PP separator delivers virtually flat voltage plateaus over 2000 h with small overpotential (4 mV), illustrating their excellent interfacial stability and outstanding cyclability. In a sharp contrast, the cells with nPG@PP display higher voltage hysteresis after 500 h (> 14 mV), and the cells with bare PP separators appear micro-short circuiting after dozens of hours (inset of Fig. 4h and Supplementary Fig. 15). When increasing the areal capacity to 5 mAh cm^{-2} or even 10 mAh cm^{-2}, the cells with mPG-12@PP separator still show stable voltage plateaus over 1700 h and 1400 h, respectively (Supplementary Fig. 16, 17). Remarkably, such an ultralong cycle life of Na anodes (~ 2000 h at 1 mA cm^{-2} and 1 mAh cm^{-2}, ~ 1700 h at 5 mA cm^{-2} and 5 mAh cm^{-2}, ~ 1400 h at 10 mA cm^{-2} and 10 mAh cm^{-2}) is superior to those of other Na anodes stabilized by various methods under similar test conditions, such as 3D MXene-melamine foam (720 h at 10 mA cm^{-2} and 10 mAh cm^{-2})[43], poly(vinylidene difluoride) coated Cu current collector (1200 h at 1 mA cm^{-2} and 1 mAh cm^{-2})[44], and Na@reduced GO anodes (300 h at 5 mA cm^{-2} and 5 mAh cm^{-2})[24], as shown as in Supplementary Fig. 18 and Supplementary Table 2[21, 45–50]. What's more, the cells with mPG-12@PP separator reveal excellent rate capability under increasing current densities up to 25 mA cm^{-2} with 25 mAh cm^{-2} (overpotential ≈ 83 mV, Fig. 4i), whereas the voltage-time curve of the cells with PP separator suffers from severe fluctuation (Supplementary Fig. 19), suggestive of the stable SEI and superior reaction kinetic of Na metal anodes with mPG-12@PP separator. To the best of our knowledge, such a ultrahigh rate performance (25 mA cm^{-2}, 25 mAh cm^{-2}) greatly surpassed to those of the state-of-the-art reported Na metal anodes stabilized by diversified strategies, such as 3D MXene-melamine foam (20 mA cm^{-2}, 20 mAh cm^{-2})[43], Na-Hg alloy (8 mA cm^{-2}, 8 mAh cm^{-2})[51], core-shell C@Sb nanoparticles (5 mA cm^{-2}, 1 mAh cm^{-2})[52], Sb_2MoO_6 microspheres (10 mA cm^{-2}, 8 mAh cm^{-2})[53], oxygen-functionalized carbon nanotube (10 mA cm^{-2}, 2 mAh cm^{-2})[14], reduced GO aerogel (5 mA cm^{-2}, 5 mAh cm^{-2})[54], Sn^{2+} pillared Ti_3C_2 MXene (8 mA cm^{-2}, 3 mAh cm^{-2})[55], porous Cu matrix (3 mA cm^{-2}, 1 mAh cm^{-2})[45], and 3D carbon felt (5 mA cm^{-2}, 2 mAh cm^{-2})[56] (Fig. 4j and Supplementary Table 3).

Electrochemical performance of Na/NVP full batteries. To highlight the applicability of mPG based separator, the Na/NVP full batteries were assembled (Fig. 5a and Supplementary Fig. 20), in which as-deposited Na metal foil (10 mAh cm^{-2}) with PG-12@PP or bare PP separator was used as the metal anode. Figure 5b exhibits the comparison of cycling stability of Na/NVP full cell with mPG-12@PP and PP separators at 1 C. Significantly, the Na/NVP cell with mPG-12@PP separator demonstrates exceptionally stable cycling performance with 90% retention of the initial capacity over 500 cycles

(Fig. 5c). While the specific capacity of Na/NVP full cell with bare PP separator decays rapidly after 120 cycles caused by the formation of Na dendrites and “dead Na”. Moreover, the full battery with mPG-12@PP separator reveals superior rate capability to that with PP separator (Fig. 5d). Specifically, the discharge capacities of the full cell with mPG-12@PP separator are 103, 96, 86 and 75 mAh g^{-1} at 1 C, 5 C, 15 C and 30 C, much higher than those of cell with PP separator (99, 91, 76 and 55 mAh g^{-1}; Fig. 5e and Supplementary Fig. 21). These results further confirm that 2D mPG based separators enable Na metal batteries with significantly enhanced Coulombic efficiency, cycling stability and rate performance.

Discussion

The outstanding performance of Na metal anodes is attributed to the reasonable design of 2D multi-functional mPG heterostructure synergistically coupled the sodiophilic polydopamine surface, 2D defective graphene and definable mesoporous structure. First, the polydopamine layer features abundant polar groups, *e.g.*, C = O, -OH and -NH-, endowing it with excellent electrolyte wettability and strong substrate adhesion to facilitate homogeneous Na ion transport and suppress the growth of Na dendrites at molecular level. Second, 2D GO with intrinsic defects, atomic thickness and excellent flexibility, offers a homogeneous Na ions delivery by this nanoporous buffer layer and enhances the mechanical strength of mPG and corresponding functional separators[25, 33]. Third, the exposed mesoporous structure not only increases the accessible contact area between active polydopamine and electrolyte, but also provides definable Na ion pathways to regulate local current density and terminate the “tip effect”. Consequently, 2D mPG heterostructures as multi-functional ion redistributors substantially realize dendrite-free uniform Na deposition from chemical molecule to physical structure levels.

In summary, 2D mPG heterostructures with definable pore size and sheet thickness have been demonstrated for ultrastable and high-capacity Na anodes. Owing to the abundant sodiophilic groups, nanoporous graphene and exposed mesoporous structure, 2D mPG heterostructures endow uniform Na ion transport and dendrite-free Na deposition, as confirmed by both theoretical and experimental analysis. Notably, the Na metal anodes with mPG-12@PP separator exhibited high Coulombic efficiency (> 99.5%), outstanding cycling stability (~ 2000 h) and landmark rate performance (25 mA cm^{-2} and 25 mAh cm^{-2}). Further, 2D mPG based separator realized high-performance Na/NVP metal batteries with exceptionally enhanced cyclability and rate capability. Therefore, this strategy paves a new avenue for the design of 2D mesoporous polymer materials towards next-generation safe, rechargeable sodium metal batteries.

Declarations

Data Availability

The authors declare that all the data supporting the findings of this study are available within the article and its Supplementary Information or from the corresponding author upon reasonable request.

Acknowledgements

The authors acknowledge the financial support from the National Key R&D Program of China (Grants 2016YBF0100100, 2016YFA0200200), National Natural Science Foundation of China (Grants 51872283, 21805273, 51925207, 51872277 and U1910210), LiaoNing Revitalization Talents Program (Grant XLYC1807153), Natural Science Foundation of Liaoning Province (Grant 20180510038), DICP (DICP ZZBS201708, DICP ZZBS201802 and DICP I202032), DICP&QIBEBT (Grant DICP&QIBEBT UN201702), Dalian National Laboratory For Clean Energy (DNL), CAS, DNL Cooperation Fund, CAS (DNL180310, DNL180308, DNL201912 and DNL201915), and the Fundamental Research Funds for the Central Universities (WK2060140026).

Author contributions

Z.-S. W., M. Y. and Y. Y. proposed and supervised the overall project. J. Q. and H. S. prepared the samples and performed the electrochemical measurements. K. H. did the FVM simulations. P. L. did the DFT simulations. P. W., F. X. and B. Y. performed the SEM and TEM measurements of materials. J. Q., H. S., K. H., M. Y., Y. Y. and Z.-S. W. analyzed the data and wrote the paper. All authors discussed the results and commented on the manuscript. All authors have given approval to the final version of the manuscript.

Additional information

Supplementary Information accompanies this paper at http://www.nature.com/naturecommunications

Competing financial interests: The authors declare no competing financial interests

Reprints and permission information is available online at http://npg.nature.com/ reprints and permissions/

How to cite this article:

Publisher's note: Springer Nature remains neutral with regard to jurisdictional claims in published maps and institutional affiliations

References

1. Goodenough J.B., Park K.S. The Li-ion rechargeable battery: a perspective. *J. Am. Chem. Soc.* **135**, 1167–1176 (2013).
2. Cheng X.B., Zhang R., Zhao C.Z., Zhang Q. Toward safe lithium metal anode in rechargeable batteries: A review. *Chem. Rev.* **117**, 10403–10473 (2017).
3. Bruce P.G., Freunberger S.A., Hardwick L.J., Tarascon J.-M. Li–O_2 and Li–S batteries with high energy storage. *Nat. Mater.* **11**, 19–29 (2012).
4. Ma L., *et al.* Dendrite-free lithium metal and sodium metal batteries. *Energy Storage Mater.* **27**, 522–554 (2020).

5. Wang Y., *et al.* Developments and perspectives on emerging high-energy-density sodium-metal batteries. *Chem* **5**, 2547–2570 (2019).
6. Sun B., *et al.* Design strategies to enable the efficient use of sodium metal anodes in high-energy batteries. *Adv. Mater.*, e1903891 (2019).
7. Lee B., Paek E., Mitlin D., Lee S.W. Sodium metal anodes: emerging solutions to dendrite growth. *Chem. Rev.* **119**, 5416–5460 (2019).
8. Fan L., Li X. Recent advances in effective protection of sodium metal anode. *Nano Energy* **53**, 630–642 (2018).
9. Vaalma C., Buchholz D., Weil M., Passerini S. A cost and resource analysis of sodium-ion batteries. *Nat. Rev. Mater.* **3**, 18013 (2018).
10. Wei S., *et al.* A stable room-temperature sodium–sulfur battery. *Nat. Commun.* **7**, 11722 (2016).
11. Hartmann P., *et al.* A rechargeable room-temperature sodium superoxide (NaO_2) battery. *Nat. Mater.* **12**, 228–232 (2013).
12. Xu X., *et al.* Quasi-solid-state dual-ion sodium metal batteries for low-cost energy storage. *Chem* **6**, 902–918 (2020).
13. Wang H., Matios E., Luo J., Li W. Combining theories and experiments to understand the sodium nucleation behavior towards safe sodium metal batteries. *Chem. Soc. Rev.* **49**, 3783–3805 (2020).
14. Ye L., *et al.* A Sodiophilic interphase-mediated, dendrite-free anode with ultrahigh specific capacity for sodium-metal batteries. *Angew. Chem. Int. Ed.* **58**, 17054–17060 (2019).
15. Hu X., *et al.* Quasi-solid state rechargeable Na-CO_2 batteries with reduced graphene oxide Na anodes. *Sci. Adv.* **3**, e1602396 (2017).
16. Lee J., *et al.* Ultraconcentrated sodium bis(fluorosulfonyl)imide-based electrolytes for high-performance sodium metal batteries. *ACS Appl. Mater. Interfaces* **9**, 3723–3732 (2017).
17. Lee Y., *et al.* Fluoroethylene carbonate-based electrolyte with 1 M sodium bis(fluorosulfonyl)imide enables high-performance sodium metal electrodes. *ACS Appl. Mater. Interfaces* **10**, 15270–15280 (2018).
18. Shim J., Kim H.J., Kim B.G., Kim Y.S., Kim D.-G., Lee J.-C. 2D boron nitride nanoflakes as a multifunctional additive in gel polymer electrolytes for safe, long cycle life and high rate lithium metal batteries. *Energy Environ. Sci.* **10**, 1911–1916 (2017).
19. Zhou W., Li Y., Xin S., Goodenough J.B. Rechargeable sodium all-solid-state battery. *ACS Cent. Sci.* **3**, 52–57 (2017).
20. Luo W., *et al.* Ultrathin surface coating enables the stable sodium metal anode. *Adv. Energy Mater.* **7**, 1601526 (2017).
21. Zhu M., *et al.* Dendrite-free sodium metal anodes enabled by a sodium benzenedithiolate-rich protection layer. *Angew. Chem. Int. Ed.* **59**, 6596–6600 (2020).
22. Wang H., Wang C., Matios E., Li W. Critical role of ultrathin graphene films with tunable thickness in enabling highly stable sodium metal anodes. *Nano Lett.* **17**, 6808–6815 (2017).

23. Liu S., Tang S., Zhang X., Wang A., Yang Q.H., Luo J. Porous Al current collector for dendrite-free Na metal anodes. *Nano Lett.* **17**, 5862–5868 (2017).
24. Wang A., *et al.* Processable and moldable sodium-metal anodes. *Angew. Chem. Int. Ed.* **56**, 11921–11926 (2017).
25. Foroozan T., *et al.* Synergistic effect of graphene oxide for impeding the dendritic plating of Li. *Adv. Funct. Mater.* **28**, 1705917 (2018).
26. Zhang C., Wang A., Zhang J., Guan X., Tang W., Luo J. 2D materials for lithium/sodium metal anodes. *Adv. Energy Mater.* **8**, 1802833 (2018).
27. Tu N.D.K., *et al.* Co-solvent induced piezoelectric γ-phase nylon-11 separator for sodium metal battery. *Nano Energy* **70**, 104501 (2020).
28. Li C., *et al.* Two-dimensional molecular brush-functionalized porous bilayer composite separators toward ultrastable high-current density lithium metal anodes. *Nat. Commun.* **10**, 1363 (2019).
29. Li N., *et al.* Normalized lithium growth from the nucleation stage for dendrite-free lithium metal anodes. *Angew. Chem. Int. Ed.* **58**, 18246–18251 (2019).
30. Kim P.J., Pol V.G. High performance lithium metal batteries enabled by surface tailoring of polypropylene separator with a polydopamine/graphene layer. *Adv. Energy Mater.* **8**, 1802665 (2018).
31. Ryou M.-H., Lee D.J., Lee J.-N., Lee Y.M., Park J.-K., Choi J.W. Excellent cycle life of lithium-metal anodes in lithium-ion batteries with mussel-inspired polydopamine-coated separators. *Adv. Energy Mater.* **2**, 645–650 (2012).
32. Ryou M.H., Lee Y.M., Park J.K., Choi J.W. Mussel-inspired polydopamine-treated polyethylene separators for high-power li-ion batteries. *Adv. Mater.* **23**, 3066–3070 (2011).
33. Shi H.D., *et al.* A two-dimensional mesoporous polypyrrole-graphene oxide heterostructure as a dual-functional ion redistributor for dendrite-free lithium metal anodes. *Angew. Chem. Int. Ed.* **59**, 12147–12153 (2020).
34. Sun T., Li Z.-j., Wang H.-g., Bao D., Meng F.-l., Zhang X.-b. A biodegradable polydopamine-derived electrode material for high-capacity and long-life lithium-ion and sodium-ion batteries. *Angew. Chem. Int. Ed.* **55**, 10662–10666 (2016).
35. Yue X., Liu H., Liu P. Polymer grafted on carbon nanotubes as a flexible cathode for aqueous zinc ion batteries. *Chem. Commun.* **55**, 1647–1650 (2019).
36. Liu T., *et al.* Self-polymerized dopamine as an organic cathode for Li- and Na-ion batteries. *Energy Environ. Sci.***10**, 205–215 (2017).
37. Liu T., Lee B., Kim B.G., Lee M.J., Park J., Lee S.W. In situ polymerization of dopamine on graphene framework for charge storage applications. *Small* **14**, e1801236 (2018).
38. Li W., Liu J., Zhao D. Mesoporous materials for energy conversion and storage devices. *Nat. Rev. Mater.* **1**, 16023 (2016).
39. Peng L., *et al.* Holey two-dimensional transition metal oxide nanosheets for efficient energy storage. *Nat. Commun.* **8**, 15139 (2017).

40. Liu S., *et al.* Patterning two-dimensional free-standing surfaces with mesoporous conducting polymers. *Nat. Commun.* **6**, 8817 (2015).
41. Li S., Jiang M., Xie Y., Xu H., Jia J., Li J. Developing high-performance lithium metal anode in liquid electrolytes: challenges and progress. *Adv. Mater.* **30**, e1706375 (2018).
42. Liang J., *et al.* A nano-shield design for separators to resist dendrite formation in lithium-metal batteries. *Angew. Chem. Int. Ed.* **59**, 6561–6566 (2020).
43. Shi H., *et al.* 3D flexible, conductive, and recyclable $Ti_3C_2T_x$ MXene-melamine foam for high-areal-capacity and long-lifetime alkali-metal anode. *ACS Nano* **14**, 8678–8688 (2020).
44. Hou Z., *et al.* Poly(vinylidene difluoride) coating on Cu current collector for high-performance Na metal anode. *Energy Storage Mater.* **24**, 588–593 (2020).
45. Wang C., Wang H., Matios E., Hu X., Li W. A chemically engineered porous copper matrix with cylindrical core-shell skeleton as a stable host for metallic sodium anodes. *Adv. Funct. Mater.* **28**, 1802282 (2018).
46. Chu C., *et al.* Uniform nucleation of sodium in 3D carbon nanotube framework via oxygen doping for long-life and efficient Na metal anodes. *Energy Storage Mater.* **23**, 137–143 (2019).
47. Guo M., *et al.* Three dimensional frameworks of super ionic conductor for thermodynamically and dynamically favorable sodium metal anode. *Nano Energy* **70**, 104479 (2020).
48. Sun B., *et al.* Dendrite-free sodium-metal anodes for high-energy sodium-metal batteries. *Adv. Mater.*, e1801334 (2018).
49. Luo W., *et al.* Encapsulation of metallic Na in an electrically conductive host with porous channels as a highly stable Na metal anode. *Nano Lett.* **17**, 3792–3797 (2017).
50. Bao C., *et al.* Sodiophilic decoration of a three-dimensional conductive scaffold toward a stable Na metal anode. *ACS Sustainable Chem. Eng.* **8**, 5452–5463 (2020).
51. Zhang Q., Hu M., He J., Liu X.Z., He G., Ding Y. A thermodynamically stable quasi-liquid interface for dendrite-free sodium metal anodes. *J. Mater. Chem. A* **8**, 6822–6827 (2020).
52. Wang G., *et al.* Core-shell C@Sb nanoparticles as a nucleation layer for high-performance sodium metal anodes. *Nano Lett.* **20**, 4464–4471 (2020).
53. Lu X., *et al.* Enabling high-performance sodium metal anodes via a sodiophilic structure constructed by hierarchical Sb_2MoO_6 microspheres. *Nano Energy* **69**, 104446 (2020).
54. Wu F., *et al.* Reduced graphene oxide aerogel as stable host for dendrite-free sodium metal anode. *Energy Storage Mater.* **22**, 376–383 (2019).
55. Luo J., *et al.* Pillared Mxene with ultralarge interlayer spacing as a stable matrix for high performance sodium metal anodes. *Adv. Funct. Mater.* **29**, 1805946 (2019).
56. Chi S.-S., Qi X.-G., Hu Y.-S., Fan L.-Z. 3D flexible carbon felt host for highly stable sodium metal anodes. *Adv. Energy Mater.* **8**, 1702764 (2018).

Figures

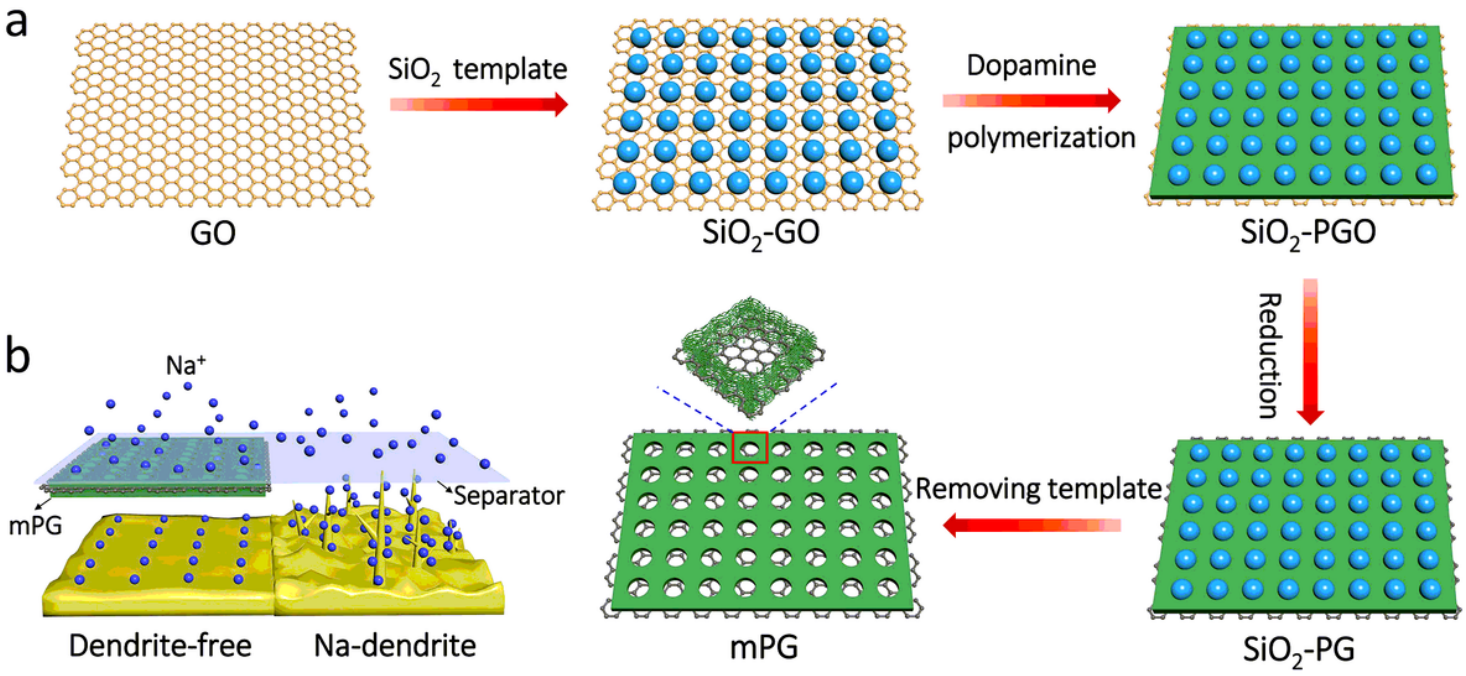


Figure 1

Scheme of 2D mPG heterostructures for dendrite-free Na metal anode. (a) Schematic of the fabrication of 2D mPG heterostructures, and (b) diagram of Na deposition behaviors with bare PP separator and mPG based PP separator.

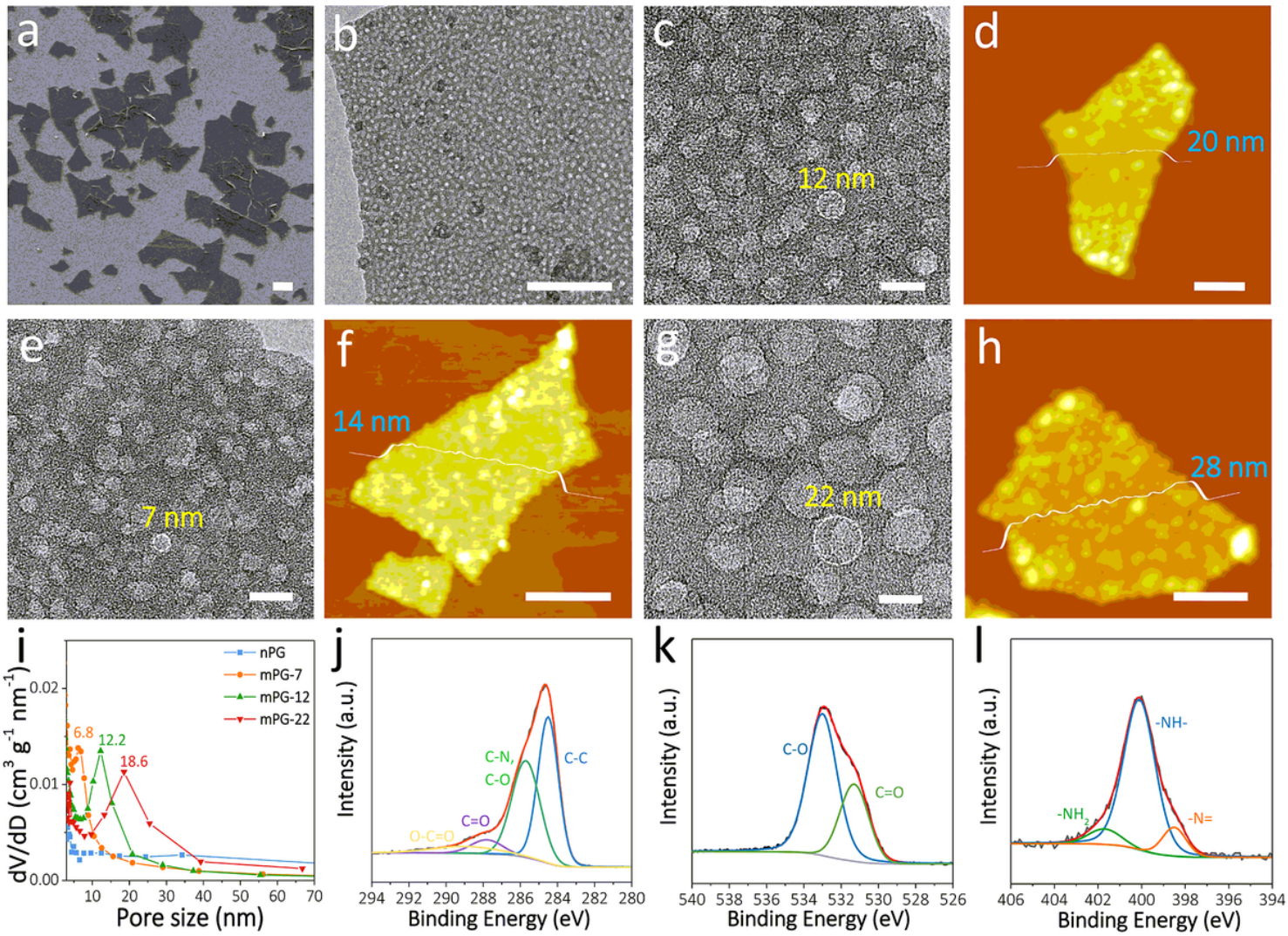


Figure 2

Characterization of 2D mPG heterostructures. (a) SEM image, (b, c) TEM and HRTEM images, (d) AFM image and corresponding thickness analysis of mPG-12 nanosheets. (e) HRTEM image, (f) AFM image and corresponding thickness analysis of mPG-7 nanosheets. (g) HRTEM image, (h) AFM image and corresponding thickness analysis of mPG-22 nanosheets. (i) The pore size distribution curves of mPG-7, mPG-12, mPG-22 and nPG nanosheets. (j-l) High-resolution XPS (j) C1s, (k) O1s, and (l) N1s spectra of mPG-12 nanosheets. Scale bars: (a) 1 μm, (b) 200 nm, (c, e, g) 20 nm, and (d, f, h) 500 nm

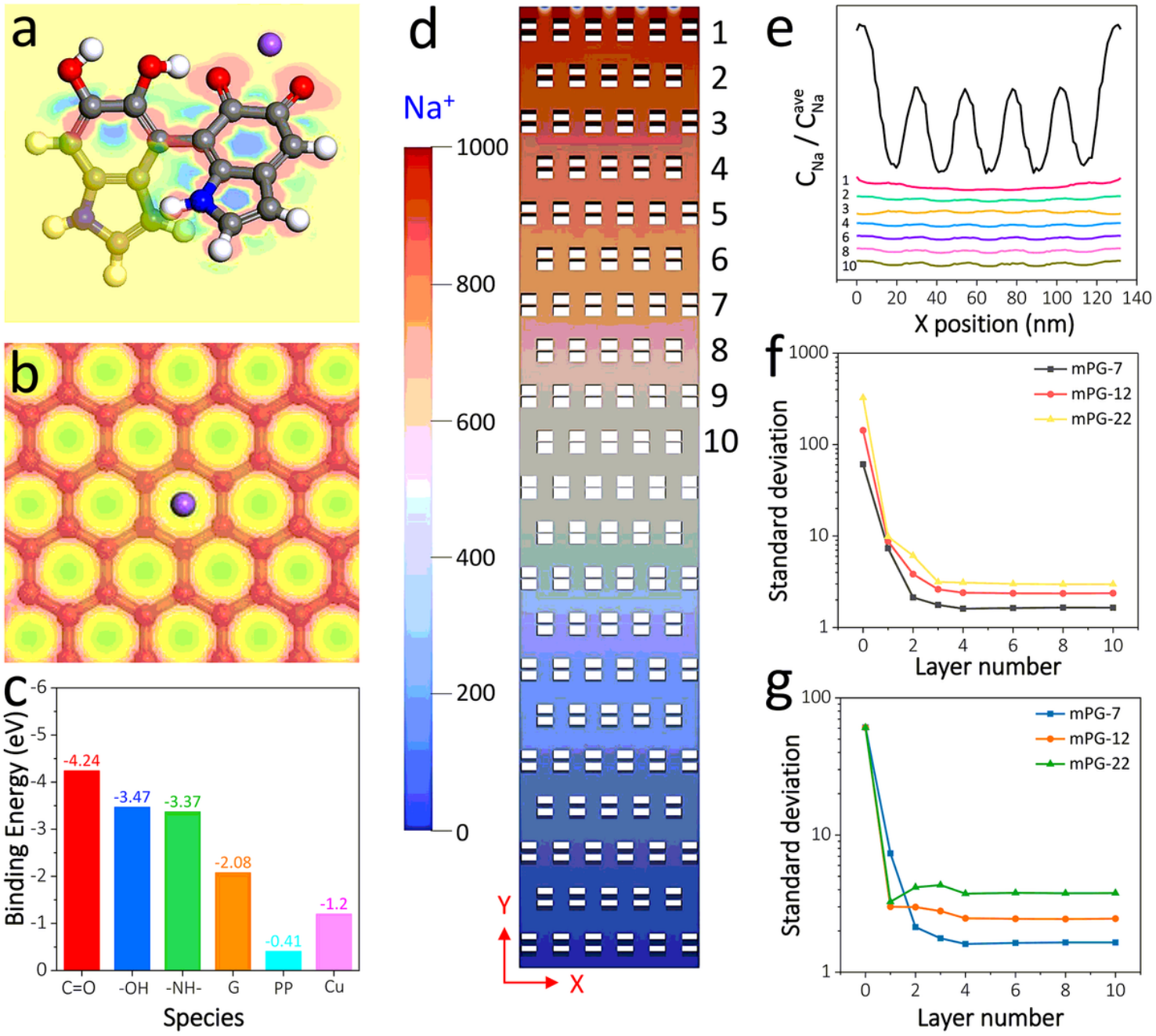


Figure 3

Sodiophilic nature and Na ion deposition behavior of 2D mPG heterostructures by DFT calculation and FEM simulation. (a) The deformation charge density of polydopamine molecule with Na. (b) The deformation charge density of graphene with Na. (c) Binding energies of Na with Cu, PP, graphene and different functional groups in polydopamine. (d) Model diagram of Na ions through mPG layer (Inset: the color represents different concentration of Na ions). (e) The relative concentration of Na ions beneath different mPG layer with same amplitude and period of Na ion distribution at the entrance. (f, g) Standard deviation of Na ion concentration beneath mPG-7, mPG-12 and mPG-22 layers with (f) same amplitude and (g) same fluctuation of Na ion distribution at the entrance.

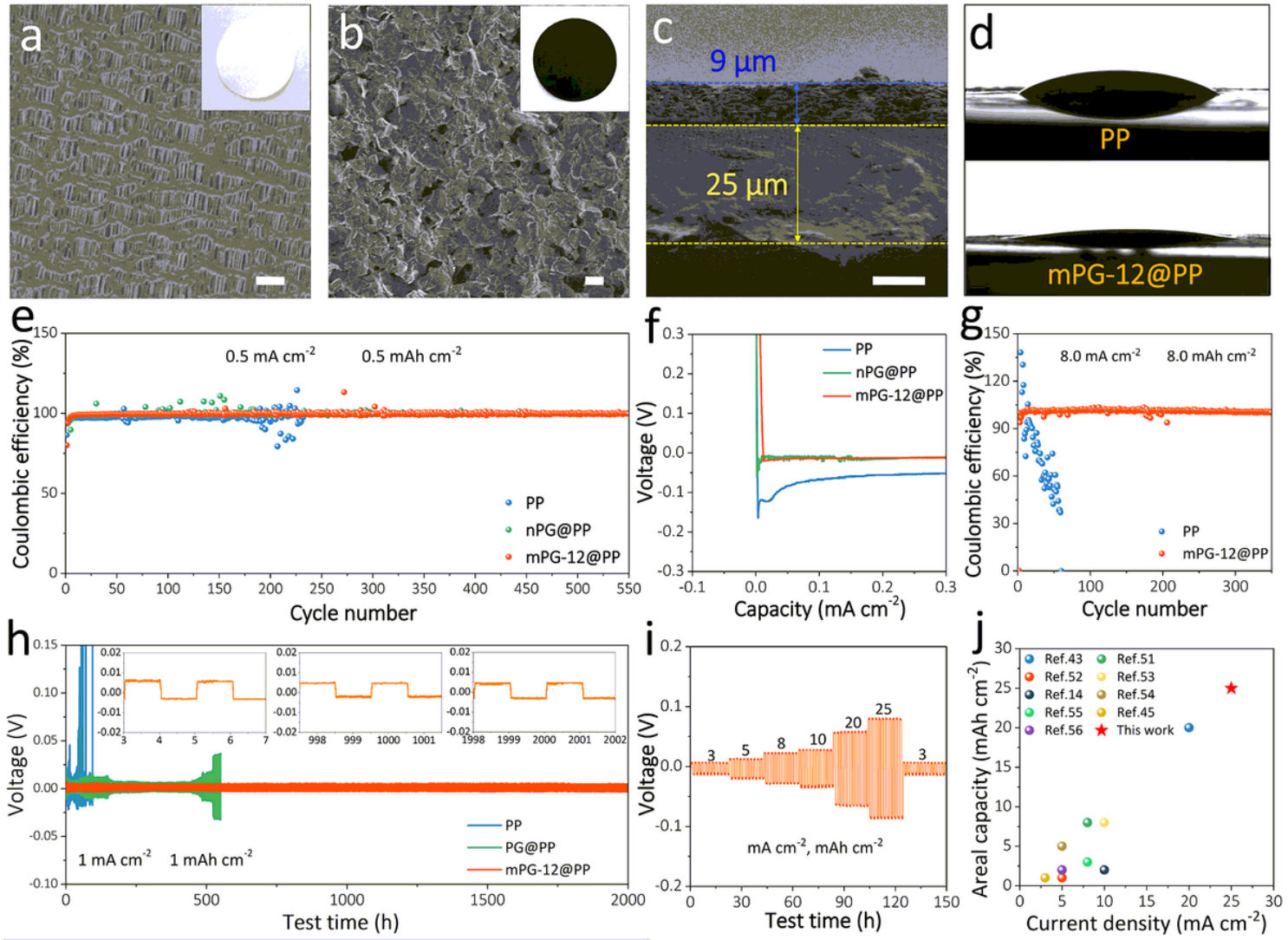


Figure 4

Characterization and performance of mPG-12@PP separator for Na metal anodes. (a) Top-view SEM image and photograph (inset) of bare PP separator. (b) Top-view SEM image and photograph (inset) of mPG-12@PP separator. (c) Cross-section SEM image of mPG-12@PP separator. (d) Contact angles of the electrolyte on bare PP (top) and mPG-12@PP (bottom) separators. (e) Coulombic efficiencies of Na/Cu cells with mPG-12@PP, nPG@PP and PP separators tested at 0.5 mA cm-2, 0.5 mAh cm-2. (f) Voltage-capacity curves during Na nucleation with different separators. (g) Coulombic efficiencies of Na/Cu cells with mPG-12@PP and PP separators measured at 8.0 mA cm-2, 8.0 mAh cm-2. (h) Voltage-time profiles of Na/Na symmetric cells with mPG-12@PP, nPG@PP and PP separators at 1 mA cm-2, 1 mAh cm-2 (insets: magnified voltage profiles of Na/Na cell with mPG-12@PP at 5, 1000 and 2000 h, respectively). (i) Rate performance of Na/Na cells with mPG-12@PP separator obtained at different current densities and capacity, respectively. (j) Rate performance comparison of Na metal anodes with other reported works recently. Scale bars: (a, b) 1 μm, and (c) 10 μm

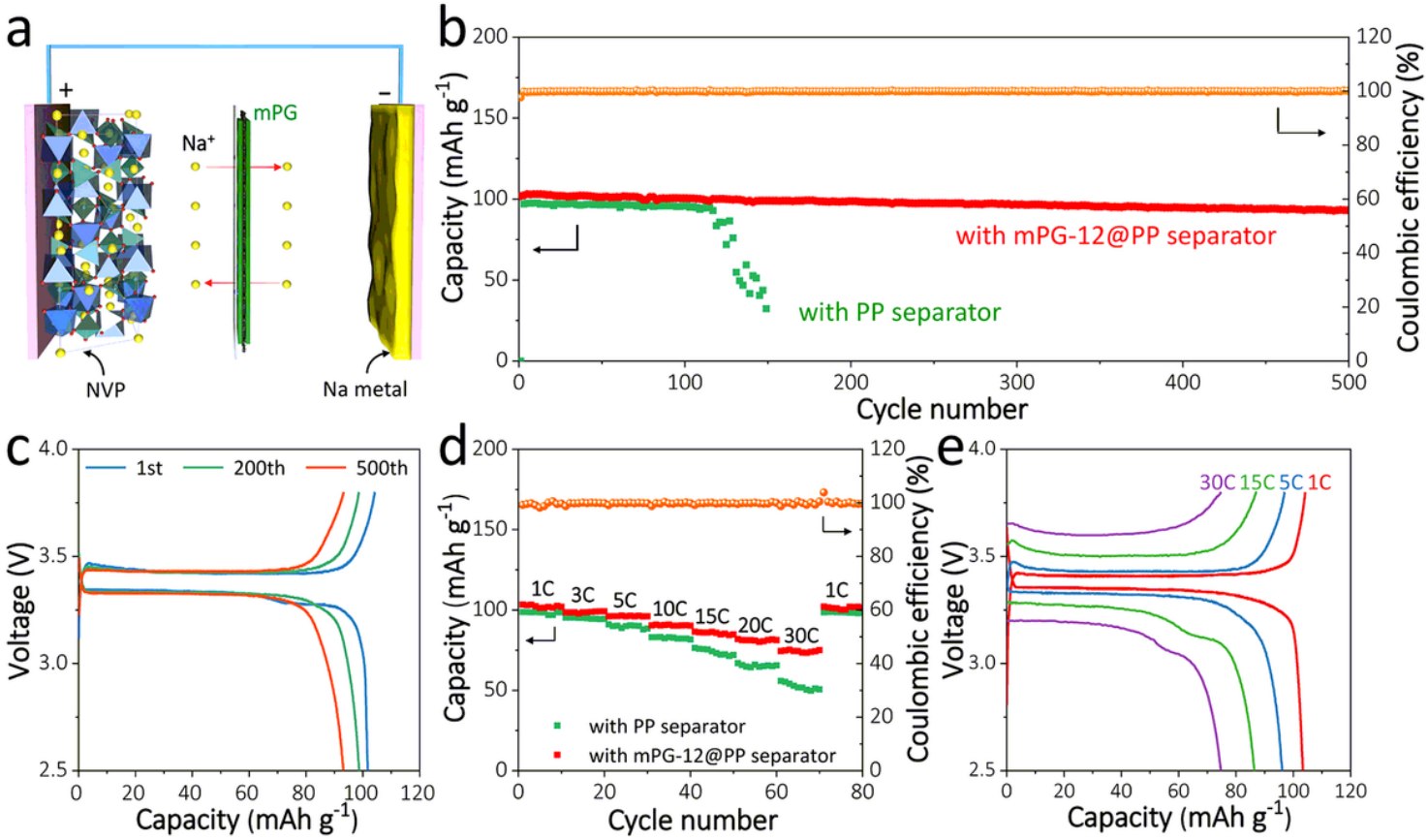


Figure 5

Electrochemical performance of Na/NVP full cells with mPG-12@PP and PP separators. (a) Schematic illustration of Na/NVP full cell with mPG based separators. (b) Cycling stability obtained at a current density of 1 C. (c) Galvanostatic charge-discharge profiles of Na/NVP full cells with mPG-12@PP separator (1st, 200th and 500th cycle). (d) Rate capability measured from 1 C to 30 C. (e) Galvanostatic charge-discharge profiles of Na/NVP full cells with mPG-12@PP separator obtained at varying current densities.

Supplementary Files

This is a list of supplementary files associated with this preprint. Click to download.

- SupportingInformation.docx